Nanoscale

PAPER

View Article Online
View Journal | View Issue

Cite this: *Nanoscale*, 2026, **18**, 11796

An interface engineered ZnO/rGO/Au NPs@MoS_2 heterojunction for enhanced photoelectrochemical DNA sensing

Asad Ali, †[a,b] Farhana Akbar Mangrio,†[a] Ammar Bin Yousaf, [c] Lixin Zhu,*[b] Xiaoliang Xu *[d] and Yongbo Song *[a]

The conventional polymerase chain reaction (PCR) method for DNA detection suffers from limited sensitivity and linearity, restricting its application to samples with molar concentrations above 10^{-2} mmol. Here, we report a highly sensitive photoelectrochemical (PEC) biosensor for detecting the PML/RARA fusion gene, a key biomarker of acute promyelocytic leukemia (APL). A biosensing interface was constructed using an 18-mer single-stranded DNA probe immobilized on a ZnO/rGO/Au NPs@MoS_2 heterojunction. The integration of three-dimensional ZnO nanoflowers with ultrathin MoS_2 nanosheets not only suppresses photogenerated electron–hole recombination but also enhances light absorption across the ultraviolet-visible (UV-vis) spectrum, thereby improving photoelectric conversion efficiency. Incorporating reduced graphene oxide (rGO) effectively reduces interfacial resistance between ZnO and MoS_2, while plasmonic Au nanoparticles (Au NPs) facilitate the absorption of visible light and the charge transfer through localized surface plasmon resonance (SPR) effects. During target recognition, a CdSe quantum dot (QD)-labeled reporter DNA(rDNA) hybridizes with the target DNA (tDNA), which specifically binds to the surface-anchored capture probe. The formation of a DNA duplex and subsequent assembly of CdSe QDs alter interfacial charge transfer and induce steric and electrostatic hindrance, leading to a concentration-dependent drop in photocurrent. Under optimized conditions, the biosensor exhibits a broad linear detection range from 100 fM to 1 μM and an ultralow limit of detection (LOD) of 1.9 fM, surpassing those of many previously reported DNA sensing platforms. Finite-difference time-domain (FDTD) simulations further confirm the contribution of plasmonic enhancement to the improved photoelectric response. This work presents a robust strategy for constructing advanced heterojunction photoelectrodes and provides a promising PEC platform for ultrasensitive biomarker detection in bioanalysis and clinical diagnostics.

Received 7th January 2026,
Accepted 4th March 2026

DOI: 10.1039/d6nr00077k

rsc.li/nanoscale

1 Introduction

The rapid and precise detection of specific DNA sequences has significantly advanced areas such as early cancer detection, viral testing, and the diagnosis of genetic disorders.[1,2] Since DNA concentration is usually very low in biological samples, it is necessary to explore an ultrasensitive technique for DNA detection with high sensitivity, simple operation, and accuracy.[3] Photoelectrochemical (PEC) bioanalysis has emerged as a powerful tool for ultrasensitive biosensing due to its low background signal, high sensitivity, simplicity, and cost-effectiveness.[4,5] PEC biosensors use light for excitation and electrical signals for detection, enabling miniaturization and simpler instrumentation.[6] In contrast, traditional analysis systems such as electrochemiluminescence, colorimetry, fluorescence, photoelectrochemistry, and polymerase chain reaction (PCR) often suffer from enzyme errors, primer interference, and nonspecific fluorescence signals.[6–8] PEC biosensors rely on photoactive materials that convert biorecognition events, *e.g.*, DNA hybridization and enzyme reactions, into measurable electrical signals, making them ideal for clinical diagnostics and environmental monitoring.

The design of PEC biosensors relies on photoactive electrodes that convert photoirradiation into an electrical signal, making the choice of photoactive materials critical. Numerous inorganic metallic semiconductors such as Cu_2O, TiO_2, CdSe, CdTe, ZnO, and ZnSe are widely used.[9–11] Among them, zinc oxide is particularly attractive due to its non-toxicity, afford-

[a]*School of Biomedical Engineering, Anhui Provincial Institute of Translational Medicine, Anhui Medical University, Hefei 230032, P. R. China. E-mail: ybsong860@ahmu.edu.cn*
[b]*Department of Surgery & Central Laboratory, The First Affiliated Hospital of Anhui Medical University, Hefei 230022, PR China. E-mail: zhulixin@ahmu.edu.cn*
[c]*Center for Advanced Materials, Qatar University, Doha 2713, Qatar*
[d]*Key Laboratory of Strongly-Coupled Quantum Matter Physics, Chinese Academy of Sciences, School of Physical Sciences, University of Science and Technology of China, Hefei, Anhui 230026, China. E-mail: xlxu@ustc.edu.cn*
† These authors contributed equally to this work.

ability, and exceptional photochemical and chemical stability. However, its wide energy band gap (3.37 eV) limits excitation to UV light,[12] restricting its direct applications in biological sensing. Morphological engineering of ZnO nanostructures is crucial for overcoming these limitations. In our previous work, 3D ZnO nanoflowers were employed instead of 1D or 2D structures, providing a significantly larger surface area for chalcogenide quantum dot deposition and improved charge separation.[13] ZnO nanoflowers, with their unique growth orientation and high surface area, will significantly enhance probe contact area and improve signal strength. Although the positive surface charge of ZnO promotes efficient DNA attachment, its limited photoelectric conversion efficiency has restricted broader application in PEC biosensing. Therefore, improving its charge conversion efficiency is essential for expanding its use in this field. Thus, to enhance photoelectric conversion efficiency, strategies such as doping, compounding, and sensitization have been explored, with sensitization being particularly practical and effective. Graphene is highly appealing due to its large surface area, excellent electrical conductivity, strong chemical stability, and outstanding mechanical strength.[14,15] Similarly, MoS_2, a transition metal dichalcogenide 2D material analogous to a graphene-like layered structure, consists of covalently bound S–Mo–S layers held together by weak van der Waals forces.[16,17] MoS_2 has large exposed active edges with high electrical conductivity that facilitates a fast charge transfer mechanism and has gained significant attention due to its remarkable optoelectronics properties, high chemical stability, high rare-earth content, and nontoxicity.[18,19] These features render MoS_2 highly promising for diverse applications spanning photovoltaics, nanoelectronics, energy storage, sensing, catalysis, and biomedical fields.[20,21] Similar to graphene and graphite, MoS_2 exhibits layer-dependent properties due to its anisotropic structure. When reduced to a monolayer or a few-layer form, MoS_2 transitions from an indirect to a direct bandgap material, significantly enhancing its photoluminescence and fluorescence quenching capabilities.[22,23] However, its intrinsic conductivity restricts the biosensing applications. To further enhance carrier dynamics, plasmonic Au nanoparticles (Au NPs) can be introduced into the heterostructure. Owing to surface plasmon resonance (SPR), Au NPs boost visible-light absorption and create hot electrons, hence enhancing photoelectric conversion efficiency.[24] In heterostructures, Au NPs serve dual roles as electron relays and photosensitizers, reducing Auger recombination while facilitating charge transfer between semiconductors of different band gaps. These properties, combined with their high surface area and biocompatibility, make Au NPs ideal for PEC biosensing applications, particularly for protein adsorption and detection. Constructing hybrid nanostructures of ZnO nanoflowers, MoS_2 nanosheets, reduced graphene oxide (rGO), and Au NPs establishes a cascade multi-heterojunction that overcomes these limitations, enabling improved interfacial charge transfer and PEC biosensing performance.

PEC sensing strategies have attracted significant interest to develop a modified photoelectrode DNA biosensor for rapid and cost-effective genetic diagnostics and other applications.[25,26] In PEC DNA biosensors, a complementary oligonucleotide capture probe is immobilized on an electrode surface, where its orientation and surface density critically determine hybridization efficiency and signal response. Target binding induces measurable changes in electrical properties, enabling sensitive detection. Consequently, the specificity and stability of the probe–target binding are critical for achieving high fidelity and reproducibility, making probe design a central challenge in DNA biosensor development. Some groups have reported several electrochemical biosensors for detecting the synthetic single-stranded (ss)-PML/RARα fusion gene using specific probes, including locked nucleic acids (LNAs),[27] CDs/GO nanocomposites,[28] dsDNA,[27] a ZnO-functionalized carbon ionic liquid electrode,[29] and poly-CCA for DNA detection.[30] In practical clinical samples, however, nucleic acids are often present as persistent double-stranded DNA or DNA/RNA complexes, which inhibit direct hybridization with surface-bound probes. Denaturation procedures can produce ssDNA; however, rapid reannealing competes with probe binding and diminishes detection performance, posing a significant obstacle to reliable biosensing.

In this work, we develop a signal-off PEC DNA biosensing strategy, in which the ssDNA sequence, primers, and complementary DNA (cDNA) of the PML–RARA fusion gene associated with acute promyelocytic leukemia (APL) were selected for analysis. Hybridization of the target PML–RARA sequence suppresses photocurrent *via* interfacial blocking and modulation of charge-transfer pathways. The degree of photocurrent quenching is directly proportional to the logarithm of the target DNA concentration, enabling ultrasensitive detection. The mechanism of synthesis and photocurrent generation in the proposed DNA assay is illustrated in Scheme 1. The ZnO/rGO/Au NPs@MoS_2 heterojunction promotes efficient separation of photogenerated electron–hole pairs, yielding enhanced and stable photocurrent. Au nanoparticles further broaden light absorption and improve charge transfer. Upon illumination, electrons transfer through the heterostructure to the fluorine-doped tin oxide (FTO) electrode, while holes are consumed by ascorbic acid (AA), preventing recombination. The negatively charged ZnO/rGO/Au NPs@MoS_2 hybrid was assembled on PDDA-treated FTO through electrostatic attraction and functionalized with thiol-terminated capture DNA. Unbound sites were blocked with 6-hydroxy-1-hexanethiol (MCH), forming a stable PEC matrix with a strong photocurrent response, enabling sensitive and specific ssDNA detection.

2 Experimental section

2.1 Synthesis of the materials

Please see the SI for the details of chemicals and reagents and synthesis of the FTO/PDDA electrode, porous 3D ZnO nanoflowers, ultrathin MoS_2 nanosheets, RGO/Au nanoparticles on ultrathin MoS_2 nanosheets, and CdSe QDs.

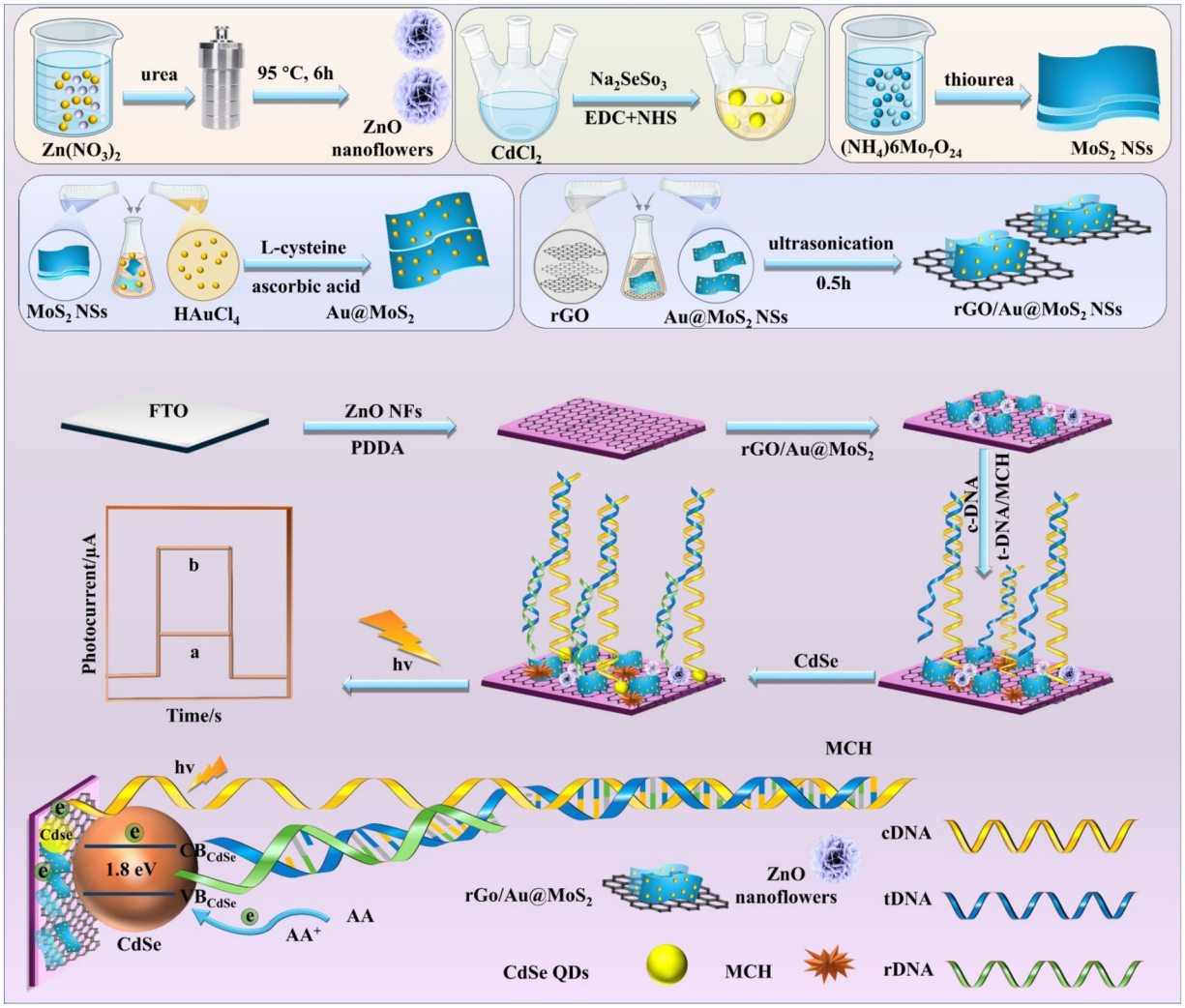

Scheme 1 Schematic representation of the fabrication of ZnO/rGO/Au NPs@MoS_2 biosensors.

2.1.1 Fabrication of the DNA biosensor. The biosensing electrode was prepared and used according to the following procedure. A 30 μL aliquot of 1 μM capture DNA (c-DNA) was first treated with 10 mM Tris-(2-carboxyethyl) phosphine (TCEP) for 1 hour at room temperature to break disulfide bonds. This pre-treated c-DNA was then incubated on the FTO/PDDA/ZnO/rGO/Au NPs@MoS_2 electrode at 4 °C overnight to facilitate immobilization. The electrode was subsequently rinsed with TE buffer (10 mM Tris-HCl, 1 mM EDTA, pH 8.0) to remove unbound c-DNA. It was then incubated with 30 μL of 1 mM 6-mercapto-1-hexanol (MCH) for 1 hour at 37 °C to passivate the surface, thereby displacing weakly adsorbed c-DNA on the electrode and blocking non-specific binding sites. The electrode was then incubated with 30 μL of target DNA (t-DNA) at varying concentrations for 100 minutes at 37 °C to allow for hybridization with the immobilized c-DNA. Following another wash with TE buffer to remove unbound strands, 30 μL of reporter DNA (r-DNA) was added and incubated to form a sandwich structure on the electrode. Afterwards, CdSe quantum dots (QDs) were introduced and covalently coupled *in situ* to the surface-bound r-DNA in the presence of 40 mg mL^{-1} EDC and 10 mg mL^{-1} NHS for 120 minutes at 37 °C. This step facilitates the covalent coupling between the amino groups of the r-DNA and the carboxyl groups of the CdSe QDs *via* EDC-NHS chemistry. Finally, the electrode was thoroughly washed with PBS buffer (pH 7.4), and the modified electrode was subjected to photoelectrochemical (PEC) detection.

2.1.2 Photoelectrochemical measurement and characterization. PEC measurements were performed with an electrochemical workstation (CHI760E) using a standard three-electrode setup. The working electrode was a modified fluorine-doped tin oxide (FTO) glass slide measuring 1 × 1 cm^2. A platinum (Pt) wire served as the counter electrode and a saturated calomel electrode (SCE) was used as the reference electrode. Electrochemical impedance spectroscopy (EIS) measurement was carried out in the same supporting electrolyte, with frequencies ranging from 1 Hz to 10^4 Hz and an applied potential

of 0.172 V *vs.* SCE. For the photocurrent tests, a blank solution comprising 0.1 M phosphate-buffered saline (PBS) at pH 7.4, containing Na_2HPO_4, NaH_2PO_4, and NaCl, along with 0.1 M ascorbic acid (AA), was used, because it acts as an effective electron donor during the PEC test. A 300 W xenon lamp with a long-wave-pass filter (cut-on wavelength of 420 nm) aligned with the AM 1.5 G spectrum supplied visible illumination to the samples. The visible light intensity was measured at 50 mW cm^{-2} using a radiometer (OPHIR, Littleton, CO). The morphologies and microstructures of the nanomaterials were characterized using a field-emission scanning electron microscope (FE-SEM; Hitachi SU-8200, Japan) operated at 15 kV. Transmission electron microscopy (TEM) images, lattice structures, *d*-spacing, elemental mappings, and distributions were analyzed with high-resolution TEM (HRTEM; JEOL JEM-1400) operated at 200 kV. The crystal structure and phases of the materials were identified *via* X-ray diffraction (XRD) spectroscopy (PANalytical X'pert Pro MRD diffractometer) with Cu Kα radiation (λ = 1.5406 Å). Surface elemental composition and valence states were studied using X-ray photoelectron spectroscopy (Thermo Scientific ESCALAB 250 spectrometer), with the XPS data calibrated to the C 1s peak at 284.6 eV. The UV-vis diffuse reflectance spectrum (DRS) was obtained with a Shimadzu UV-3700 UV-Vis-NIR spectrometer (Shimadzu Co).

3 Results and discussion

3.1 Surface morphology and composition studies

Scanning electron microscopy (SEM) and transmission electron microscopy (TEM) were used to examine the morphology and microstructure of the synthesized sensor materials. The three-dimensional shapes of the as-prepared ZnO and MoS_2 were created using a hydrothermal method. The 3D hierarchical flower-like structures of ZnO and MoS_2 are observed in the SEM images. These architectures are precisely engineered to provide a large specific surface area for photocatalytic reactions and biomolecule immobilization. This surface area is significantly higher than those of flat 2D films or solid nanoparticles. This extensive surface area allows immobilization of a substantial amount of cDNA on the sensor surface. Higher cDNA loading results in a higher reaction rate with the target analyte, producing a stronger and more sensitive signal. The ZnO exhibits a three-dimensional (3D) flower-like shape measuring a few micrometers across, as shown in Fig. 1a and b, and also in S1 and S2. A closer cross-sectional view of a single ZnO structure (Fig. 1c and d) reveals that these flowers consist of many self-assembled, porous nanoplates with typical thicknesses of approximately 119 nm. These nanoflowers have a uniform structure and large petals, which increase their specific surface area compared to traditional nanostructures such as nanorods or nanoneedles. Additionally, the numerous pores within the nanosheets form a porous network architecture. The porosity of the ZnO nanostructure at various scales ensures excellent mass transport and efficient light harvesting. It provides an effective, permeable matrix that facilitates the diffusion of the target analyte deep into the sensor, enabling it to reach the immobilized enzymes. This results in a faster response time. This characteristic is expected to improve reactant diffusion and provide a larger accessible surface area, making it especially beneficial for photocatalytic biosensing applications. TEM characterization of ultrathin MoS_2 nanosheets and Au nanoparticle-decorated rGO/MoS_2 heterostructures is shown in Fig. 1e and f. The high-resolution TEM (HRTEM) images in Fig. 1g and h reveal well-defined lattice fringes at the interfaces between Au nanocrystals and MoS_2 nanosheets. By modulating the synthesis temperature, the reaction process enables controlled disorder engineering, leading to expanded interlayer spacings, such as the 0.94 nm visible in Fig. 1h, and an increased density of active sites. Elevated temperatures promote the formation of nanodomains with short-range atomic order arranged in a quasi-periodic manner. These domains enable rapid interdomain electron transport across the basal plane because of dangling bonds that serve as active sites, a finding supported by previous XRD analyses by Xie *et al.*[31,32] Their work demonstrated that tuning the disorder level in MoS_2 nanosheets optimizes the balance between active site availability and electrical conductivity for electrocatalytic applications. Thus, tailoring these disordered nanodomains is essential for aligning the electronic and structural properties of MoS_2, thereby enhancing photoelectrochemical biosensing performance. The morphology of rGO and ssrGO/Au NPs@MoS_2 nanocomposites was also investigated *via* TEM. The rGO sheets exhibited mono- to few-layered structures (Fig. 1f and g), serving as three-dimensional conductive scaffolds that promote electron transport between photoexcited Au NPs@MoS_2 and rGO through wrinkle-induced tunneling. The persistence of these structures after ultrasonic treatment confirms strong interfacial interactions and successful heterostructure formation. The SAED pattern of the materials is presented in Fig. 1i. Furthermore, incorporating Au nanocrystals modifies charge transfer dynamics, substantially enhancing the PEC response. As visible in Fig. 1f, Au nanoparticles are densely and uniformly dispersed over the folded rGO and MoS_2 nanosheets. High-resolution imaging shows a lattice fringe spacing of 0.237 nm, corresponding to the (111) plane of Au, confirming the successful synthesis of the rGO/Au NPs@MoS_2 nanocomposite (Fig. 1h).

3.2 Structural elucidation and optical measurement

X-ray diffraction (XRD) analysis was employed to examine the crystal phases of pristine ZnO nanoflowers and the complex rGO/Au NPs@MoS_2/CdSe nanocomposite. As shown in Fig. 2, the XRD patterns display a series of strong and weak diffraction peaks at 2θ values of 26.40°, 31.74°, 33.66°, 34.34°, 36.18°, 37.74°, 44.10°, 51.53°, 54.49°, 56.64°, 61.61°, and 65.54°, which correspond to the characteristic crystallographic planes of the individual components, thereby confirming the formation of the nanocomposite material. After depositing ZnO on the fluorine-doped tin oxide (FTO) substrate, the reflections at 31.74°, 34.34°, and 36.18° are clearly assigned to the (100),

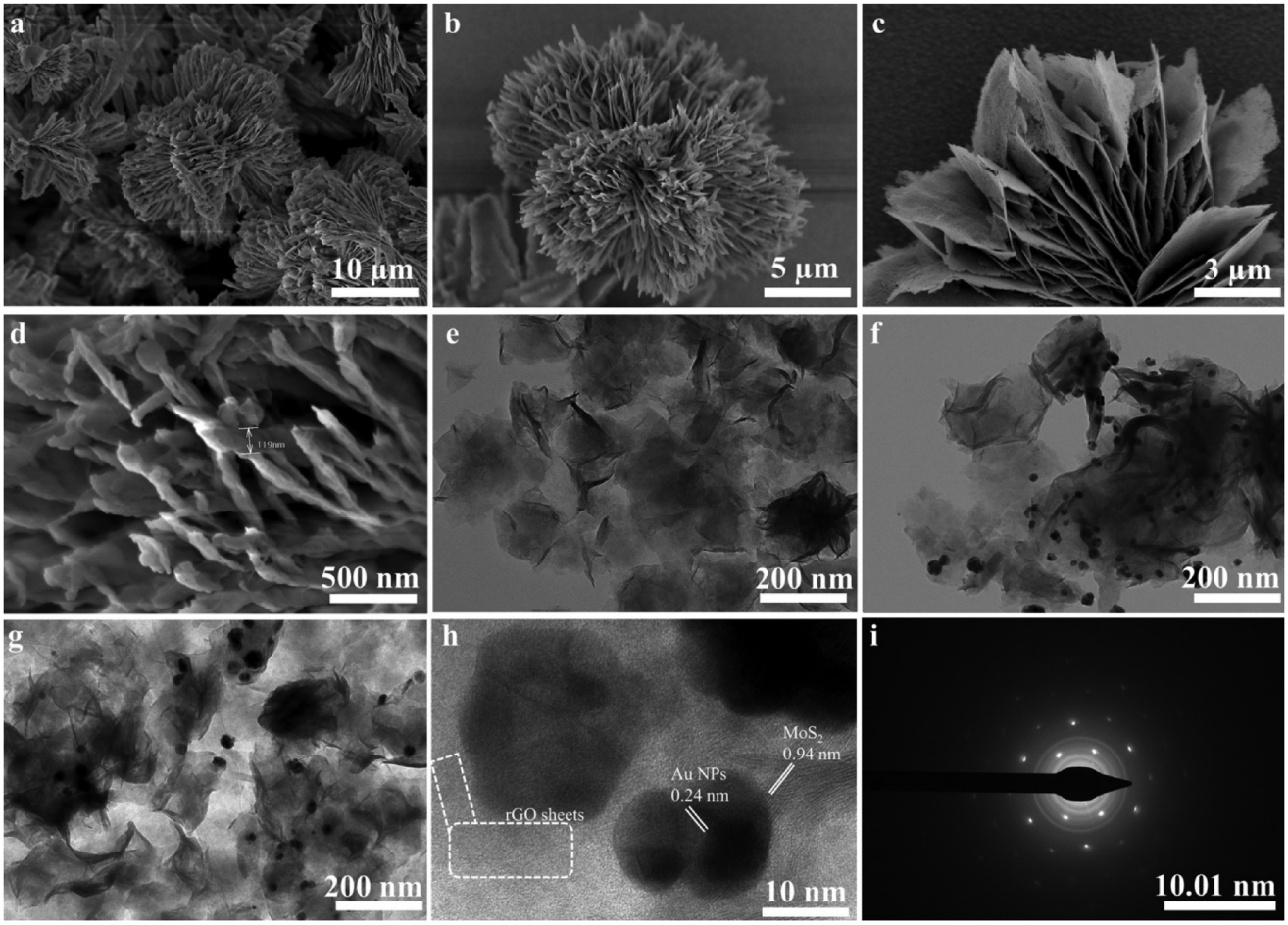

Fig. 1 FE-SEM images of (a–d) porous three-dimensional ZnO nanoflowers and (d) cross-sectional view of ZnO nanoflowers. TEM images of (e) ultrathin MoS_2 nanosheets and (f) Au NPs decorated on the rGO/MoS_2 nanosheets, (g and h) HRTEM images of Au NPs decorated on the rGO/MoS_2 nanosheets, and (i) SAED pattern of ZnO nanoflowers.

(002), and (101) planes of the hexagonal wurtzite structure of ZnO (JCPDS No. 36-1451). Notably, the (002) reflection exhibits a much higher relative intensity than the standard powder pattern. This increase in intensity indicates a preferred crystal growth orientation along the [001] direction (*c*-axis), a common feature of vertically aligned nanostructures. Peaks marked with triangles in the XRD pattern originate from the FTO substrate (JCPDS No. 46-1088).[32] Characteristic diffraction peaks of CdSe QDs are absent, likely due to their high dispersion, low concentration, or extremely small size, making them nearly undetectable by XRD. The deposition of Au nanoparticles (NPs) produces a weak, broad peak at 2θ = 44.10°, corresponding to the (200) plane of metallic gold (JCPDS No. 04-0784). The significant broadening of this peak indicates a small crystallite size, consistent with the nano-scale dimensions confirmed by TEM analysis. This broadening is a typical result of the Scherrer equation, where crystallites smaller than 10 nm produce notably wider diffraction peaks.[33] The MoS_2 component, synthesized *via* a hydrothermal process with controllable disorder engineering, exhibits a characteristically broadened peak centered at approximately $2\theta \approx 33.66°$. This peak can be indexed to the (100) plane of the pristine 2H-MoS_2 phase (JCPDS No. 65-7025), confirming the retention of its basal plane atomic arrangement. However, the significant peak broadening, which intensifies with lower synthesis temperatures, directly reflects the introduced structural disorder, decreased crystallinity, and the formation of oxygen-incorporated MoS_2 nanosheets. Lastly, the composite pattern shows no clear diffraction peak for reduced graphene oxide (rGO). This is a common trait for graphene-based materials that have been exfoliated. It is usually due to the low stacking order and thin layer thickness of the rGO sheets below the instrument's detection threshold.

The UV-vis absorption spectra of the porous flower-like ZnO and Au NPs@MoS_2 nanocomposites with variable contents were investigated to elucidate the interaction between the probes and the substrate, which plays a crucial role in photoelectrochemical (PEC) signal transduction. The absorption peaks in the UV region are characteristic of ZnO, with the pure porous ZnO nanoflowers exhibiting a maximum absorption edge at approximately 372 nm. To clarify the energy transfer mechanisms within the system, the absorption features of the

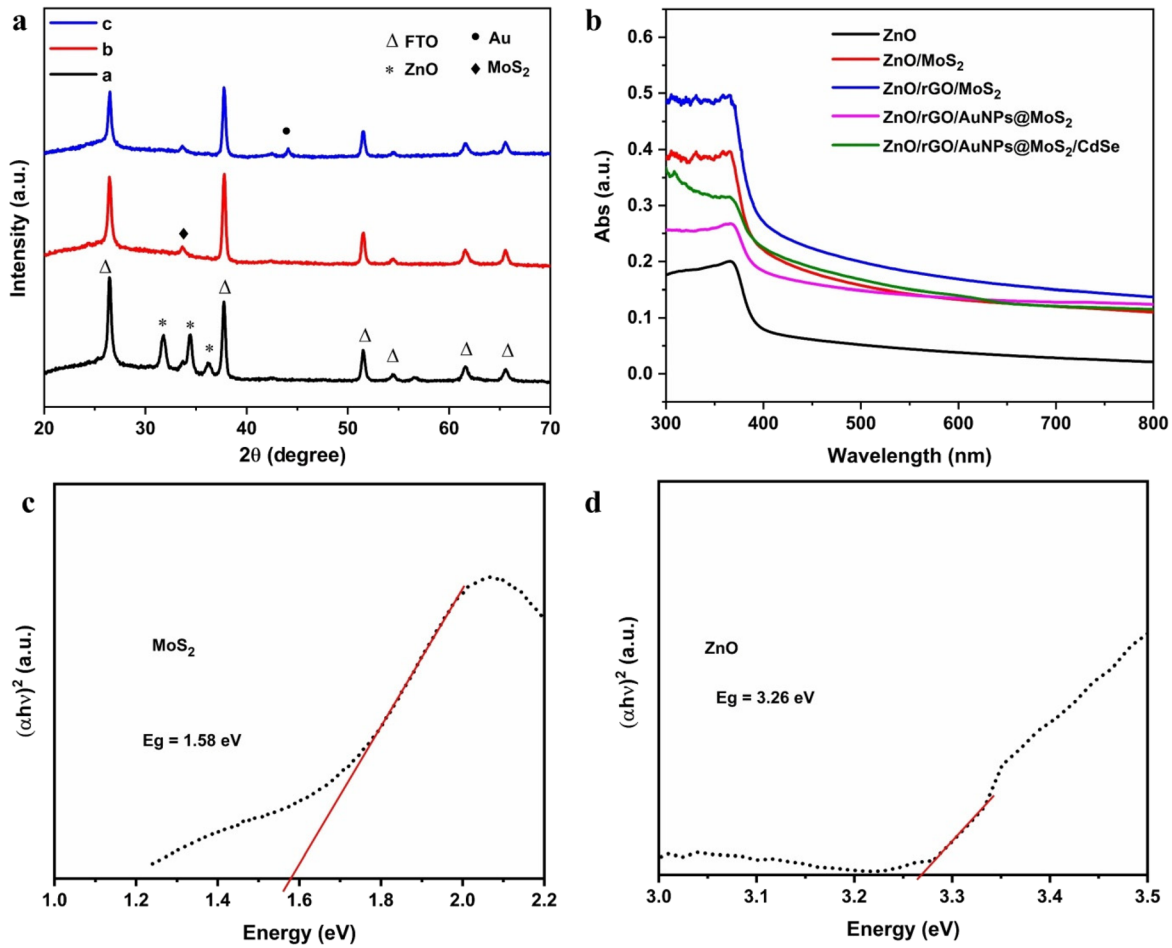

Fig. 2 XRD patterns of (line a) porous flower-like ZnO nanostructures on the FTO substrate, (line b) ZnO/rGO/MoS_2, and (line c) ZnO/rGO/Au NPs@MoS_2/CdSe QDs. (b) UV-Vis diffuse reflectance spectra of the pristine ZnO and nanocomposite materials and (c) the corresponding plots of $(ah\nu)^2$ *versus* $h\nu$ of MoS_2 and (d) $(ah\nu)^2$ *versus* $h\nu$ of ZnO.

ZnO/rGO/Au NPs@MoS_2 substrate and the p-DNA/CdSe QD probes were examined (Fig. 2b). A comparison between pure ZnO and the ZnO/rGO/Au NPs@MoS_2 nanocomposite reveals that the deposition of Au nanoparticles and rGO significantly enhances light absorption across the UV-vis range. This enhancement is attributed to the localized surface plasmon resonance (LSPR) effect of Au NPs and the excellent light-harvesting capability of rGO. Furthermore, a substantial overlap in light absorption is observed between ZnO/MoS_2 and the final ZnO/rGO/Au NPs@MoS_2/CdSe QD nanocomposite. This spectral overlap suggests a potential PEC mechanism where Au NPs and CdSe QDs competitively consume light energy and the electron donor (ascorbic acid, AA). This competition is anticipated to produce a strong quenching of the photocurrent response. As illustrated in Scheme 1, the presence of rGO and Au NPs@MoS_2, owing to their large specific surface area and superior electrical conductivity, augments the competitive capacity of the CdSe QDs. Additionally, the energy band gaps of MoS_2 nanosheets and ZnO nanoflowers are estimated to be 1.58 eV and 3.26 eV, respectively, based on the Tauc plots in Fig. 2c and d. All these optical properties confirm the successful construction of the designed PEC DNA biosensor.

X-ray photoelectron spectroscopy (XPS) was used to analyze the surface electronic states and chemical composition of the ZnO/rGO/Au NPs@MoS_2/CdSe composite electrode. The survey spectrum confirms the presence of Zn, Cd, Mo, O, S, Au, GO, and Se elements, confirming the successful synthesis of the high-purity composite, as depicted in Fig. 3a. All binding energies were calibrated using the adventitious C 1s peak referenced at 285.3 eV. The Mo 3d spectrum (Fig. 3b) shows doublet peaks at 229.16 eV (Mo $3d_{5/2}$) and 232.35 eV (Mo $3d_{3/2}$), indicating the predominance of Mo^{4+} in the products.[34] Additionally, the S 2s peak appears at 226.01 eV binding energy in MoS_2. The S 2p spectrum reveals peaks at 161.35 eV (S $2p_{3/2}$) and 162.41 eV (S $2p_{1/2}$), confirming the presence of S^{2-} ions and the successful formation of MoS_2. The peaks for Mo^{4+} and S^{2-} ions indicate the chemical coordination. Compared with reported values for the individual components, slight binding-energy shifts are observed in several core levels of the composite. The Mo $3d_{5/2}$ peak at 229.16 eV and the S

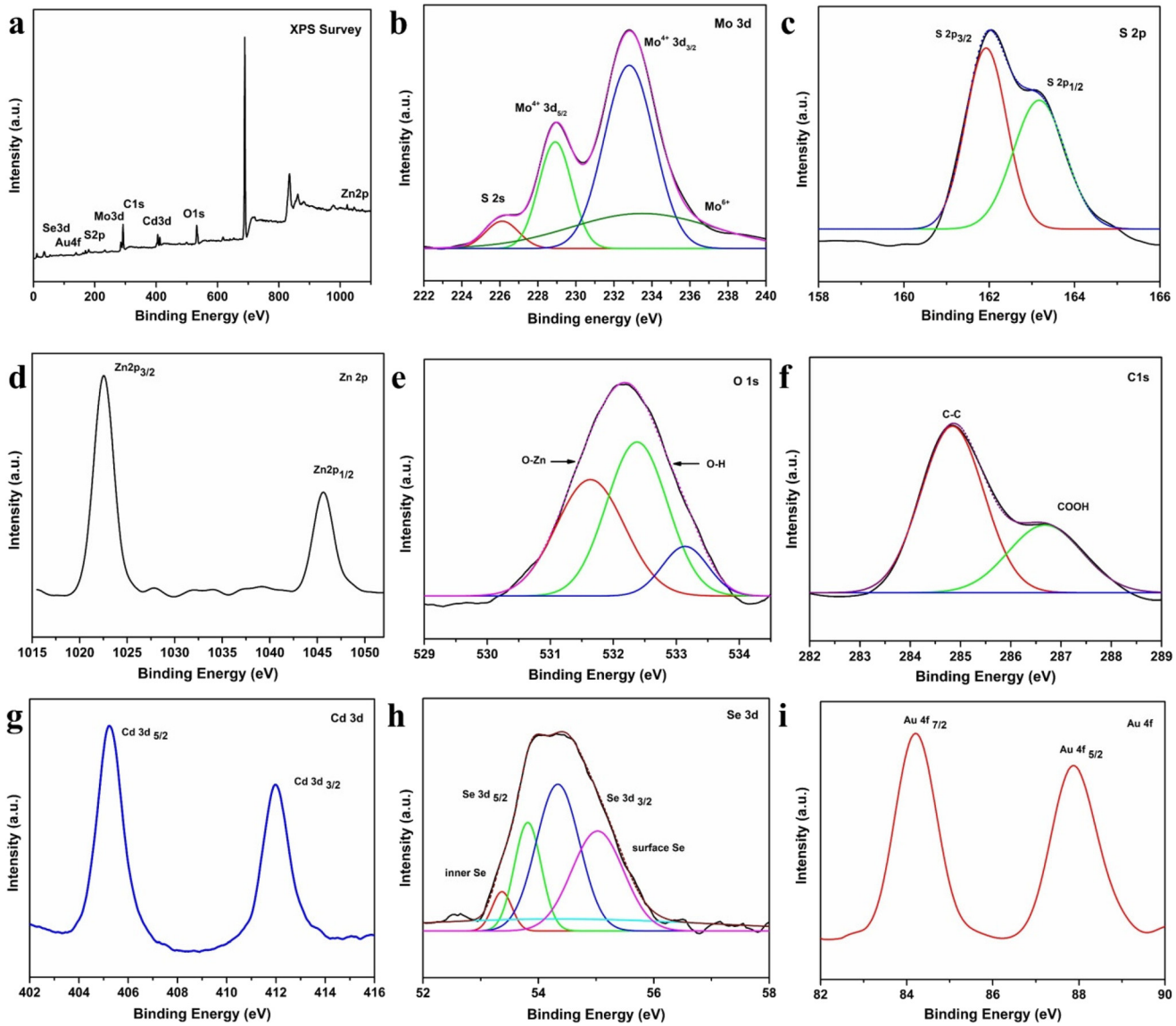

Fig. 3 XPS spectra of ZnO/rGO/Au NPs@MoS_2/CdSe: (a) XPS survey spectrum and (b) Mo 3d, (c) S 2p, (d) Zn 2p, (e) O 1s, (f) C 1s, (g) Cd 3d, (h) Se 3d, and (i) Au 4f XPS spectra.

$2p_{3/2}$ peak at 161.35 eV exhibit subtle deviations relative to pristine MoS_2, indicating modulation of the Mo–S electronic environment due to interfacial coupling. The Zn 2p spectrum shows symmetric peaks at 1021.5 eV (Zn $2p_{3/2}$) and 1044.6 eV (Zn $2p_{1/2}$), indicating the presence of Zn^{2+} in ZnO. Deconvolution of the O 1s spectrum (Fig. 3e) reveals two components; the prominent peak at 530.9 eV corresponds to lattice oxygen in Zn–O bonds. Similarly, the Zn $2p_{3/2}$ peak at 1021.5 eV shows a slight shift compared with that of bare ZnO, suggesting electronic interaction between ZnO and adjacent components. In contrast, the smaller peak at 531.8 eV is attributed to adsorbed oxygen species or surface hydroxyl groups. Here, it is worth noting that surface hydroxyls can generate primary active hydroxyl radicals capable of trapping photo-induced electrons and holes, making them essential for photocatalysis and biosensing. In Fig. 3f, the composite C 1s spectrum shows a significant reduction in the intensity of oxygen-functionalized carbon peaks (C–O and O═C–O) compared to pristine GO and the near-absence of the C═O peak, demonstrating the effective reduction of GO to RGO during the hydrothermal process.[35] The Cd 3d spectrum (Fig. 3g) presents a doublet at 405.14 eV (Cd $3d_{5/2}$) and 411.83 eV (Cd $3d_{3/2}$) with a spin–orbit splitting of 6.69 eV, confirming the Cd^{2+} oxidation state.[35] Correspondingly, the Se 3d spectrum in Fig. 3h shows peaks at 53.6 eV and 54.3 eV of Se $3d_{5/2}$ and Se $3d_{3/2}$, respectively, characteristic of Se^{2-}, which collectively verify the presence of CdSe in the composite material.[36] In Fig. 3i, the Au 4f spectrum shows peaks at 84.18 eV (Au $4f_{7/2}$) and 87.88 eV (Au $4f_{5/2}$), verifying the metallic nature of the incorporated Au nanoparticles.[34] The Au $4f_{7/2}$ peak at 84.18 eV also displays a

minor shift from standard metallic Au (≈84.0 eV), implying charge redistribution at the Au/semiconductor interface. In addition, the Cd 3d and Se 3d peaks corresponding to Cd^{2+} and Se^{2-} remain well-defined but exhibit slight binding-energy adjustments, reflecting electronic communication between CdSe and the surrounding heterostructure. These coordinated peak shifts across Mo, S, Zn, Au, Cd, and Se core levels indicate interfacial charge transfer and electron redistribution among ZnO, rGO, Au NPs, MoS_2, and CdSe. Such electronic coupling is characteristic of heterojunction formation and supports the existence of strong interfacial interaction within the composite.

3.3 PEC mechanism of the DNA biosensor

The operating principle of the PEC biosensing platform, based on the ZnO/rGO/Au NPs@MoS_2 heterostructure, is illustrated in Fig. 4. The detection mechanism relies on the modulation of the photocurrent signal, which is governed by efficient interfacial charge separation and transfer processes within the engineered heterojunction. From an energy-band perspective, the enhanced performance originates from a favorable staggered band alignment among the composite materials. Here, ZnO, an n-type semiconductor, has a more negative conduction band (CB) potential than MoS_2, enabling spontaneous transfer of photogenerated electrons from MoS_2 to ZnO upon contact with the electrode. Meanwhile, the holes migrate toward MoS_2 *via* Au nanoparticle bridges and are scavenged by ascorbic acid (AA). The highly conductive rGO serves as an electron-transport mediator between ZnO and MoS_2, accelerating carrier migration and suppressing recombination. Au nanoparticles, owing to their high work function, form Schottky junctions with MoS_2 and ZnO, generating internal electric fields that promote directional carrier separation and suppress recombination. As a result, a cascade charge-transfer pathway is established in the ZnO/rGO/AuNPs@MoS_2 multiheterojunction. This double-heterojunction (ZnO–Au and Au–MoS_2) configuration ensures efficient spatial separation of charge carriers, resulting in a stable, amplified anodic photocurrent baseline. This process is further influenced by the presence of the target analyte. Under illumination, ZnO nanoflowers (NFs) generate electron–hole pairs (e^-/h^+). The efficient interfacial band alignment facilitates rapid electron extraction and hole scavenging, thereby minimizing recombination losses. The sensing interface is modified when the target DNA hybridizes with its complementary probe. The attachment of CdSe quantum dots to the DNA duplex confirms successful hybridization. The presence of CdSe QDs substantially modifies energy transfer dynamics. The excited states of MoS_2 nanosheets interact with the surface plasmon resonance (SPR) of Au NPs, inducing an exciton–plasmon interaction (EPI). This interaction directs excited electrons from MoS_2 into the high-energy SPR states of Au. Consequently, this process disrupts the established charge-transfer pathway. Importantly, the hot electrons generated *via* SPR on the Au surface are injected into the electrolyte rather than transferred to the electrode, where they react with oxidized ascorbic acid (AA^+). This sequence creates a positive feedback loop that consumes charge carriers intended for photocurrent generation. The combined effect of impeding electron transfer at the heterojunctions and diverting charges into electrolyte reactions significantly diminishes the anodic photocurrent. Furthermore, a quenching effect was also observed as the photocurrent decreases progressively with increasing target DNA concentration. Therefore, the biosensor operates *via* a signal-off PEC mechanism, where photocurrent quenching quantitatively correlates with target concentration.

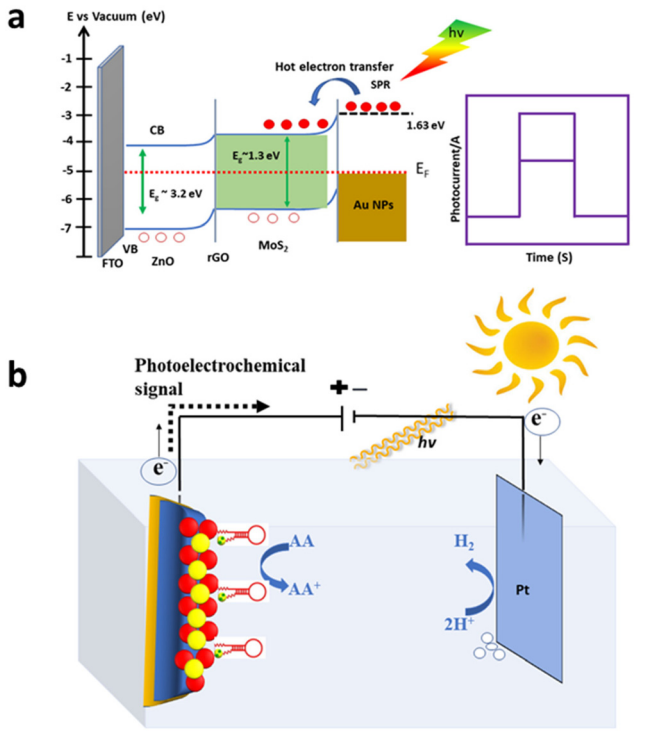

Fig. 4 (a) The mechanism of the energy band levels and energy transfer processes of the photoelectrochemical DNA sensing strategy. CB: conduction band. VB: valence band. E_F: Fermi energy. (b) A scheme showing the photoelectrochemical sensing strategy for the detection of DNA.

3.4 Photocurrent characterization of the DNA biosensor

The photoelectrochemical performance of the DNA biosensor was characterized by comparing the photocurrent responses of various modified electrodes under identical conditions, as depicted in Fig. 5a. The pristine ZnO nanoflowers on a bare FTO substrate exhibited a baseline photocurrent of 7.8 μA (curve 1). Coupling ZnO with rGO and MoS_2 to form a ZnO/rGO/MoS_2 nanocomposite significantly enhanced the photocurrent to 33.7 μA (curve 2), a 4.3-fold increase. This enhancement is attributed to the high electron mobility and conductivity of rGO, which facilitates charge transport, and the abundant catalytic active edge sites of the MoS_2 nanosheets. The photoelectrochemical performance was further optimized by introducing Au nanoparticles to create the ZnO/rGO/Au NPs@MoS_2 nanocomposite, which yielded the highest photocurrent of 48.2 μA (curve 3). This superior performance stems

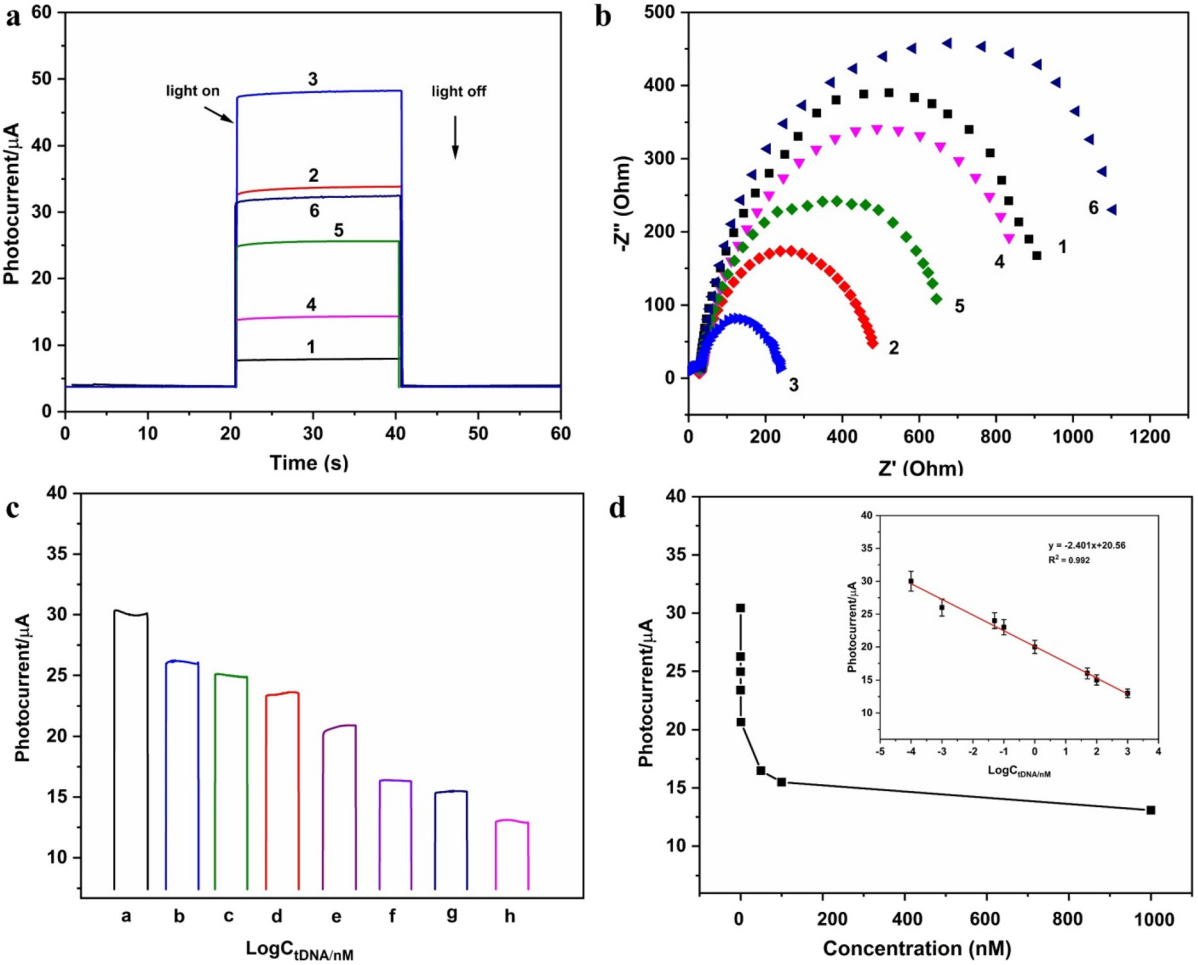

Fig. 5 (a) Photocurrent response and (b) EIS Nyquist diagram of the sensing platform of (1) ZnO NFs, (2) ZnO/rGO/MoS_2, (3) ZnO/rGO/Au NPs@MoS_2, (4) ZnO/rGO/Au NPs@MoS_2-MCH-cDNA, (5) ZnO/rGO/Au NPs@MoS_2-MCH-cDNA-tDNA, and (6) ZnO/rGO/Au NPs@MoS_2-MCH-cDNA-tDNA-rDNACdSe QDs. (c) Photocurrent responses of the PEC DNA biosensor to different concentrations of t-DNA from (a–h) 100 fM, 1 pM, 50 pM, 100 pM, 1 nM, 50 nM, 100 nM to 1 μM and (d) the corresponding calibration curve of the DNA sensor for the detection of different concentrations of the target DNA from 100 fM to 1 μM.

from the localized surface plasmon resonance (LSPR) of Au NPs, which injects "hot electrons" into the conduction band of ZnO upon illumination. This process drastically improves charge conductivity, accelerates charge transfer, and effectively suppresses charge carrier recombination. Subsequent biosensor assembly steps confirmed its successful fabrication. The immobilization of capture DNA (c-DNA) and blocking with mercaptohexanol (MCH) insulates the electrode surface, resulting in a drop in photocurrent to 14.3 μA (curve 4) due to the poor charge-transfer properties of these organic layers. Hybridization with the target DNA (t-DNA) partially restored the signal to 25.6 μA (curve 5), indicating the formation of a conductive DNA duplex. To observe the signal, a reporter DNA (r-DNA) conjugated with CdSe quantum dots (QDs) was hybridized to the captured t-DNA. The subsequent photocurrent reached 32.4 μA (curve 6), confirming the successful binding and high-efficiency sensitization by the CdSe QDs, which facilitates electron injection and inhibits electron–hole recombination. These systematic changes in photocurrent response demonstrate the successful development and sensitive signaling mechanism of the DNA biosensor.

3.5 Electrochemical impedance spectroscopy characterization of the DNA biosensor

Electrochemical impedance spectroscopy (EIS) was employed to characterize the interface properties and monitor the step-by-step fabrication process of the DNA biosensor. The resulting Nyquist plots and Bode plots of the pristine materials and multiheterojunctions are presented in Fig. 5b and Fig. S3. Each spectrum features a semicircular region, and the diameter of which corresponds to the electron-transfer resistance (R_{et}), reflecting the probe's kinetics of the redox at the electrode interface. The bare ZnO/FTO electrode exhibited a significant R_{et} value (curve 1). Upon modification with reduced graphene oxide and MoS_2, the R_{et} decreased substantially (curve 2), attributed to the excellent electrical conductivity of these materials, which facilitates electron transfer. A further decrease in R_{et} was observed after the incorporation of Au

nanoparticles (curve 3), a consequence of their high conductivity and electrocatalytic properties. Therefore, the Nyquist plot reveals a markedly reduced charge-transfer resistance for the ZnO/rGO/AuNPs@MoS_2 photoanode with a smaller curvature than that of pristine ZnO and its binary counterparts, indicating faster interfacial electron transport. This is attributed to the surface plasmon coupling mechanism in the heterojunction photoanode. To analyze the interfacial charge-transfer dynamics, Bode phase analysis was also performed. Fig. S3b illustrates that the characteristic maximum frequency (f_{max}) of the Au-modified ZnO/rGO/MoS_2 photoanode moves significantly to lower frequencies than the other photoanodes. As the electron lifetime (τ) is inversely proportional to the characteristic frequency peak ($\tau = 1/2\pi f_{max}$), this lower frequency shift corresponds to a long electron lifetime. The prolonged carrier lifetime implies reduced interfacial charge recombination and increased charge-separation efficiency in the heterostructure. The coupling of Au NPs improves charge transfer kinetics and stabilizes photogenerated carriers, thereby enhancing the PEC performance of the photoanode. In a similar fashion, the subsequent steps in biosensor fabrication increased the interfacial resistance. The immobilization of the c-DNA sequence and blocking with MCH molecules caused a pronounced increase in R_{et} (curve 4). This is due to the insulating nature of the organic layers and the electrostatic repulsion between the negatively charged DNA phosphate backbone and the anionic redox probe, $[Fe(CN)_6]^{3-/4-}$. Hybridization with the target DNA (t-DNA) resulted in a marginal further increase in R_{et} (curve 5), consistent with the addition of a second, weakly conductive DNA layer. Finally, the binding of probe DNA-functionalized CdSe quantum dots (p-DNA/CdSe QDs) led to a remarkable increase in R_{et} (curve 6), comparable to or exceeding that of the c-DNA/MCH layer. This substantial increase originates from the increased negative surface charge contributed by the QDs and their associated DNA, which electrostatically repel the anionic $Fe(CN)_6^{3-/4-}$ redox probe, thereby impeding interfacial electron transfer. Moreover, the large QD–DNA assembly introduces significant steric hindrance, further limiting charge transfer across the electrode/electrolyte interface. The systematic, step-dependent evolution of the R_{et} value confirms the successful fabrication of the DNA biosensor at each stage. The signal amplification of PEC DNA detection is based on DNA hybridization. The photocurrent signal response is directly related to the concentration of the target DNA. Fig. 5c shows the photocurrent signal of the designed PEC DNA biosensor incubated with different concentrations of the target DNA. The sensitization effect would disappear after DNA hybridization, and the photocurrent gradually decreased with increasing concentration of the target DNA. Therefore, the control experiment also demonstrates the amplification of a photocurrent signal. The calibration curve was created by plotting ΔI (where $\Delta I = I_0 - I$; I_0 is the photocurrent response when the target DNA concentration is zero and I is the photocurrent response at various DNA concentrations) against $\log C$ (C represents different target DNA concentrations), as depicted in Fig. 5d. The calibration regression equation was $\Delta I = 20.56 - 2.401 \log_{10}$ CDNA (nM), with a strong negative correlation coefficient of 0.992. The linear detection range was from 100 fM to 1 μM, with a detection limit of 1.9 fM at 3σ (where σ is the relative standard deviation of five parallel measurements at a target DNA concentration of 0). This performance was significantly better than that reported in some previously published studies (Table S1). The sensitivity of our DNA assay was compared with previous PEC findings, and the results are presented in Table S2. The photocurrent decreases as DNA concentration increases because hybridized dsDNA forms an insulating layer that blocks electron transfer. This ultrasensitive limit of detection (LOD) indicates a highly efficient PEC transduction mechanism and effective signal suppression caused by DNA binding.

3.6 Optimization conditions of the PEC biosensor

To achieve optimal PEC sensing performance, key experimental parameters were systematically optimized. These included the concentration of the FTO/ZnO/rGO/Au NPs@MoS_2 nanocomposite, the incubation times for both CdSe QDs and target DNA hybridization, and the applied bias potential. The concentration of the ZnO/rGO/Au NPs@MoS_2 nanocomposite dispersion significantly influences light absorption and charge transfer efficiency. As shown in Fig. 6a, the photocurrent intensity increased with nanocomposite concentrations from 0.5 to 2.0 mg mL^{-1}. This enhancement is due to improved light harvesting and the formation of more effective heterojunctions that facilitate charge separation. However, the photocurrent decreased at concentrations above 2.0 mg mL^{-1}, likely because of increased surface charge recombination and higher electron transfer resistance from a thicker, less efficient film. Therefore, a 2.0 mg mL^{-1} concentration was chosen for all subsequent electrode fabrication. The incubation time for t-DNA hybridization was optimized to ensure complete binding with the c-DNA probe. Fig. 6b shows that the photocurrent response, which decreases upon hybridization due to steric hindrance and electrostatic repulsion, reached a minimum plateau after 100 minutes, indicating saturation of the hybridization process. Hence, 100 minutes was selected as the optimal t-DNA incubation time. Similarly, the incubation time for CdSe QDs, which serve as a signal-amplifying label, was optimized to 120 minutes to ensure maximum attachment to the dsDNA complex (Fig. 6c). As shown in Fig. 6d, the applied bias voltage was examined. Under light illumination, the photocurrent intensity was the highest and then reached a plateau, most stable at 0 V. This potential provides a sufficient driving force for efficient electron–hole separation and charge collection without promoting significant side reactions, making it the optimal operating voltage for PEC detection.

3.7 Selectivity, reproducibility, and stability of the PEC biosensor

In addition, the practical applications of biosensors depend on the electrodes' selectivity, reproducibility, and stability in their photoresponsive characteristics. The PEC biosensor's

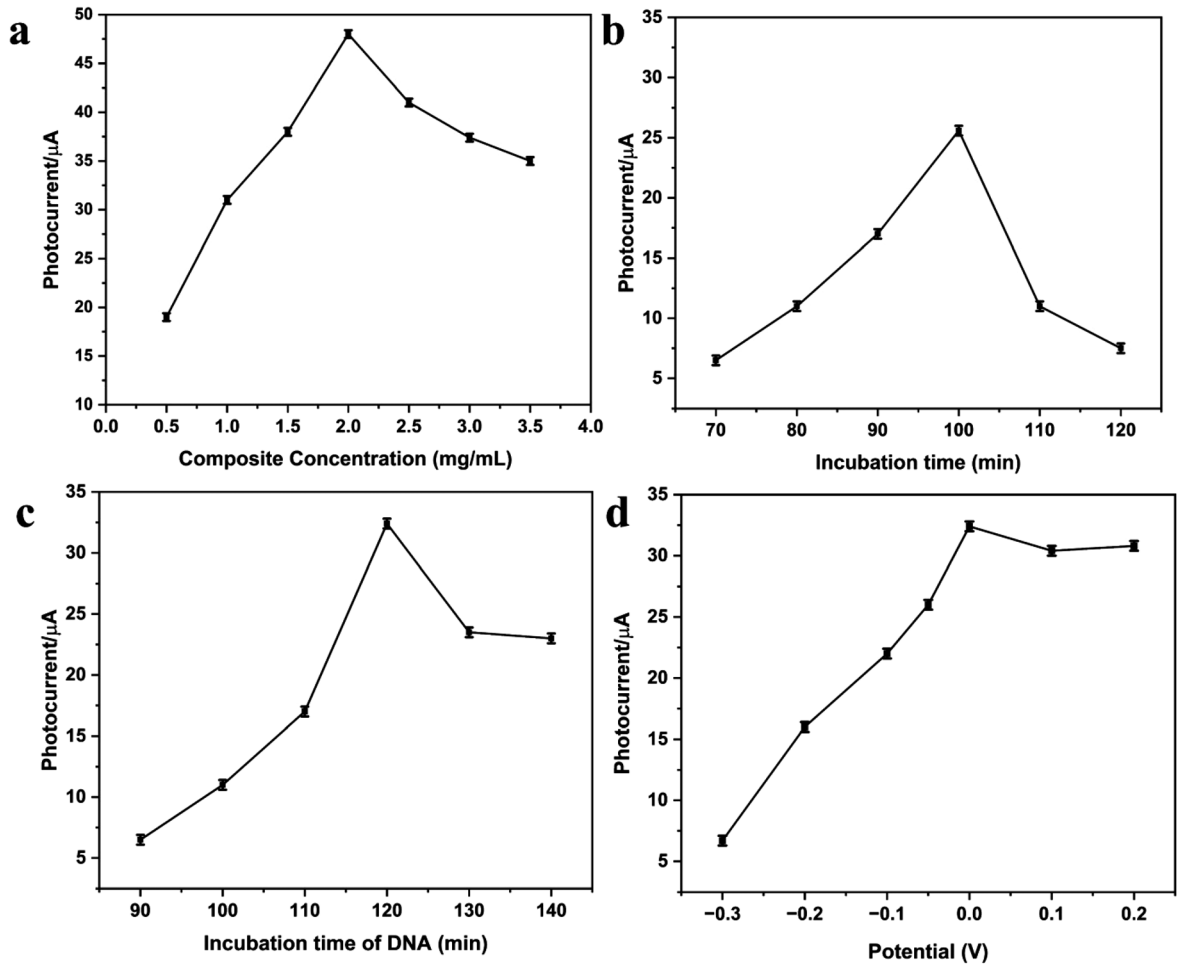

Fig. 6 (a) PEC signal response of photocurrent at different ZnO/rGO/Au NPs@MoS_2 concentrations (0.5–3.5 mg mL^{-1}). (b) Effect of incubation time of t-DNA hybridization. (c) The incubation time of r-DNA with CdSe QDs and (d) the applied voltage on the sensor performance (error bar = RSD (n = 3)).

selectivity was tested with t-DNA (a), one-base mismatched DNAI (b), and non-complementary DNA (nDNA) (c) at the identical concentration (2 μM). Fig. S4a depicts that the t-DNA gives a significantly higher photocurrent response compared to DNAI and nDNA. The much lower weak signals from DNAI and nDNA indicate that hybridization of the probe DNA to the fully complementary t-DNA is efficient. These findings confirm the great selectivity of the suggested PEC biosensing platform. Five separate photoelectrodes were used to determine t-DNA in order to assess the biosensor's reproducibility. The photocurrents of five electrodes, as depicted in Fig. S4b, are largely consistent with one another and exhibit only minor variations, with a relative standard deviation (RSD) of 2.3%. This indicates that the biosensor is highly reproducible. We also investigated the stability of the PEC DNA biosensor. The final PEC photoelectrode response was recorded under 20 seconds on/off irradiation cycles. The results show that the photocurrent remained stable and exhibited no obvious change, indicating excellent biosensor stability, as shown in Fig. S4c.

3.8 FDTD simulations

The finite-difference time-domain (FDTD) method solves Maxwell's time-dependent curl equations to simulate the temporal and spatial evolution of electromagnetic waves within a finite computational domain containing arbitrarily shaped structures. This approach was employed to theoretically validate the energy transfer process by visualizing the spatial distribution of the photoinduced electric field and the corresponding photocurrent density generated under different detector configurations.[37] To study the properties of composite materials, we used a finite-time-domain difference method to simulate the optoelectronic magnetic field of the coupled structure based on materials under incident light in the 300 nm–750 nm range, as depicted in Fig. 7. We found that the internal field strength distribution of MoS_2 and rGO is weaker than that of zinc oxide, which is related to their high electron mobility. Additionally, the gold particles' locations show a higher field strength distribution due to plasmon exci-

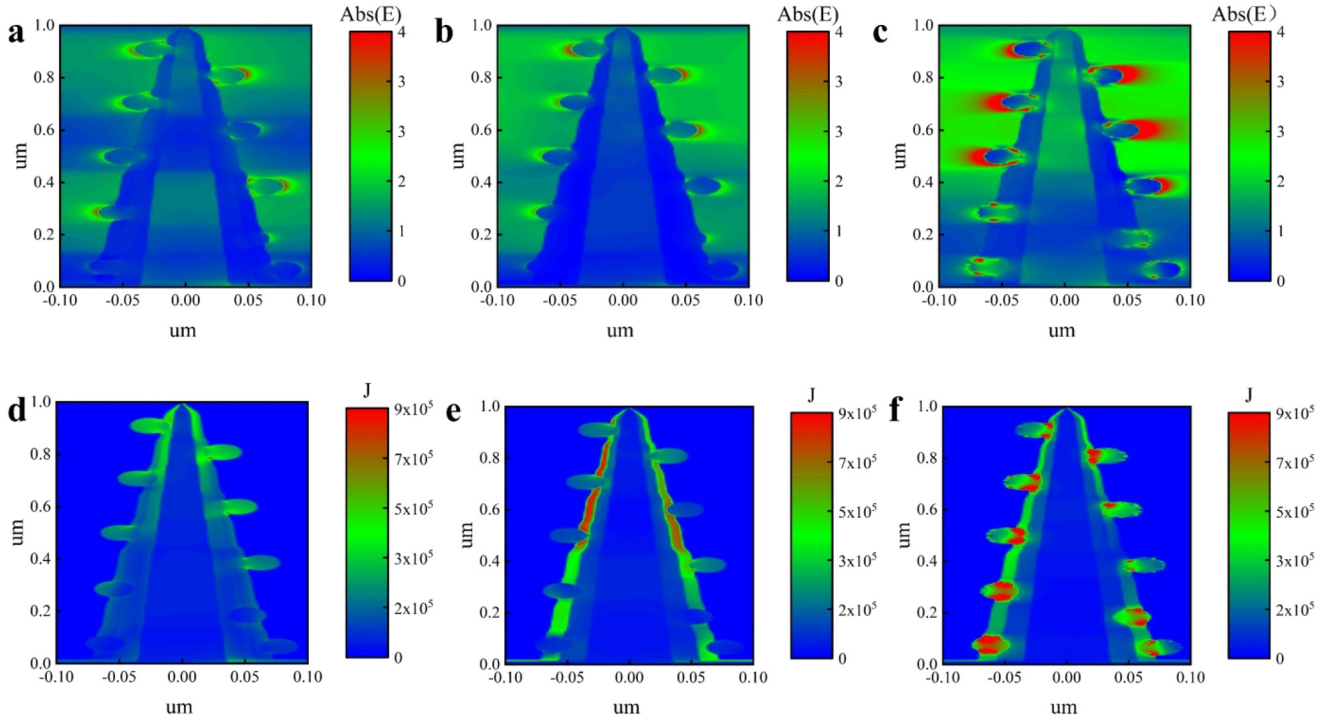

Fig. 7 FDTD simulation of (a–c) electric field distributions and (d–f) photocurrent density distributions of ZnO nanoflowers and the rGO/Au NPs@MoS_2 electrode.

tation, where gold exhibits surface plasmon resonance with the incident light field. This resonance produces a large scattering cross section that enhances the local electric field, increasing the absorption and utilization of incident light. Since the current reflects the detected information, we analyzed the current density of the structure under illumination. We observed that the photocurrent is mainly distributed in the outermost layer of the material, which is beneficial for detecting external information. The increasing current density from inside to outside indicates that our structure favors carrier transmission, resulting in higher detection accuracy. A composite layered nanoflower structure with a height of more than 300 nm was established on FTO glass. The nano flower has three layers of materials: zinc oxide, rGO, and MoS_2, which are composed of four-nanometer pieces with a length of 1 μm. The nanoflowers are loaded with nanosphere particles with a radius of 15 nm.

4 Conclusions

In this study, an improved photoelectrochemical (PEC) biosensor was developed for highly sensitive and precise detection of single-stranded DNA (ssDNA). The sensor design featured a compact three-dimensional (3D) nanostructure made of ZnO nanoflowers integrated with the active edge sites of ultrathin MoS_2 nanosheets, combined with reduced graphene oxide (rGO) and plasmonic Au nanoparticles, and further co-sensitized with CdSe quantum dots (QDs). The ZnO/rGO/Au NPs@MoS_2 heterostructure creates an efficient two-dimensional (2D) photoactive interface that enhances light absorption, charge separation, and transport. XPS analysis confirmed the successful formation of the hybrid composite, while XRD, TEM, SEM, and EIS characterization studies verified its structural stability and interfacial coupling. The co-sensitization effect between CdSe QDs and the nanocomposite electrode significantly enhanced photoinduced charge transfer, leading to a substantial amplification of the PEC response. The optimized biosensor exhibited a broad linear detection range and an extremely low detection limit, surpassing many previously reported PEC DNA platforms. The excellent sensing performance was due to the combined effects of the plasmonic Au nanoparticles and the highly conductive rGO interface, which reduced electron–hole recombination and boosted photoelectric conversion efficiency. FDTD simulations further verified the plasmonic enhancement and light-harvesting capabilities of the heterojunction. Overall, this work offers a strategic approach for constructing high-performance PEC biosensors through interface engineering and plasmonic coupling. The ZnO/rGO/Au NPs@MoS_2-based heterostructure presents a promising pathway for ultrasensitive DNA detection and has significant potential for early diagnosis of DNA-related diseases and biomolecular monitoring.

Conflicts of interest

There are no conflicts to declare.

Data availability

All data supporting the findings of this study are available within the article and its supplementary information (SI). The supplementary information contains additional experimental details, chemicals and materials, L-type PML/RARA Fusion Gene, SEM, Nyquist and Bode plots, Table S1. Comparison of PEC sensors, Table S2. Comparison of this work PEC DNA bioassay, selectivity, reproducibility, and stability of the biosensors. See DOI: https://doi.org/10.1039/d6nr00077k.

Additional raw data that support the plots within this paper are available from the corresponding author upon reasonable request.

Acknowledgements

The authors thank the National Natural Science Foundation of China for supporting this work through grants, no. 51872279 and 52072005. A. Ali gratefully acknowledges funding from Anhui Medical University, P.R. China, *via* the Youth Researcher Cultivation Fund (grant no. 0601163201). The authors thank the Department of Surgery and Central Laboratory at The First Affiliated Hospital of Anhui Medical University and the Micro Nano Functional Lab of the Department of Physics at the University of Science and Technology of China for providing valuable assistance with our experiments.

References

1 H. Deng, Y. Chai, R. Yuan and Y. Yuan, In Situ Formation of Multifunctional DNA Nanospheres for a Sensitive and Accurate Dual-Mode Biosensor for Photoelectrochemical and Electrochemical Assay, *Anal. Chem.*, 2020, **92**, 8364–8370.

2 D. Long, M. Li, H. Wang, H. Wang, Y. Chai, Z. Li and R. Yuan, Ultrasensitive Photoelectrochemical Assay for DNA Detection Based on a Novel SnS_2/Co_3O_4 Sensitized Structure, *Anal. Chem.*, 2020, **92**, 14769–14774.

3 H. Li, M. Han, X. Weng, Y. Zhang and J. Li, DNA-Tetrahedral-Nanostructure-Based Entropy-Driven Amplifier for High-Performance Photoelectrochemical Biosensing, *ACS Nano*, 2021, **15**, 1710–1717.

4 J. Fu, D. Leng, J. Chen, X. Ren, Y. Li, T. Wu, Q. Wei and B. Cai, Advanced Dual-Mode Microfluidic Sensing Platform Based on Amphiphilic Polymer-Capped Perovskite Nanozymes Induced Photoelectrochemical Signal Amplification and Fluorescence Emission, *Anal. Chem.*, 2025, **97**, 1386–1394.

5 H.-J. Li, C. Huang, F. Wang, Y. Shen, L. Jin, Q. Feng, X. Chen, Q. Liao, M. Zhu, D. Wang, X. Hou and B. He, Photo-Nanozyme-Integrated Photoelectrochemical-Electrochemical Dual-Mode Biosensor: Enabling Amplification-Free Detection of miRNA-133a in Acute Myocardial Infarction, *Anal. Chem.*, 2025, **97**, 6686–6693.

6 J. Sun, L. Li, S. Ge, P. Zhao, P. Zhu, M. Wang and J. Yu, Dual-Mode Aptasensor Assembled by a WO_3/Fe_2O_3 Heterojunction for Paper-Based Colorimetric Prediction/Photoelectrochemical Multicomponent Analysis, *ACS Appl. Mater. Interfaces*, 2021, **13**, 3645–3652.

7 X.-B. Hu, Y.-L. Wang, J.-L. Lv, M.-Y. Zheng, S.-H. Ma, J.-T. Cao and Y.-M. Liu, A Chemical Redox Cycling-Based Dual-Mode Biosensor for Self-Powered Photoelectrochemical and Colorimetric Assay of Heat Shock Protein, *ACS Sens.*, 2025, **10**, 196–203.

8 Y. Dong, W. Wang, C. Ye and Y. Song, Recent advances in photoelectrochemistry-coupled dual-modal biosensors: From constructions to biosensing applications, *Nano Res.*, 2024, **17**, 5512–5528.

9 D. Jiang, C. Ma, L. Zeng, N. Xu, Y. Zhou, X. Xu, M. Yang and L. Zhu, A novel PEC biosensor based on dual SPR induced fluorescence and electron transfer co-quenching, *Mater. Today Chem.*, 2025, **47**, 102832.

10 A. Ali, F. A. Mangrio, B. Qu, A. u. Rashid, S. A. Hussain, L. Zhu, Y. Shen and L. Chen, Advanced plasmonic few-layered InSe nanosheet heterojunctions for enhanced photoelectrochemical water splitting, *Mater. Res. Bull.*, 2025, **182**, 113172.

11 L. Chen, H. Jiang, F. Liu, S. A. Hussain, H. Chamkouri, Y. Song, P. Chen, A. Ali and X. Wang, ZnSe/ZnS Core/Shell Quantum Dots with Narrow Emission Bands for QLED Displays, *ACS Appl. Opt. Mater.*, 2025, **3**, 1800–1809.

12 Y. Yue, Y. Zhou, H. Dong, Z. Liu, M. Xu, Y. Xu, Y. Sun, T. Wang and X. Wang, "Signal-On" Photoelectrochemical Biosensor Based on CdS Quantum Dot/ZnO and Ag Nanoparticles for Sensitive Determination of Interleukin-6, *ACS Appl. Nano Mater.*, 2025, **8**, 15495–15503.

13 A. Ali, X. Li, J. Song, S. Yang, W. Zhang, Z. Zhang, R. Xia, L. Zhu and X. Xu, Nature-Mimic ZnO Nanoflowers Architecture: Chalcogenide Quantum Dots Coupling with $ZnO/ZnTiO_3$ Nanoheterostructures for Efficient Photoelectrochemical Water Splitting, *J. Phys. Chem. C*, 2017, **121**, 21096–21104.

14 S. Sengupta and M. Kundu, 2H-1T WS_2/rGO/MWCNT Nanocomposites for High-Performance Supercapacitors, *ACS Appl. Nano Mater.*, 2025, **8**, 15452–15462.

15 H. Zheng, Y. Lu, K. H. Ye, J. Hu, S. Liu, J. Yan, Y. Ye, Y. Guo, Z. Lin, J. Cheng and Y. Cao, Atomically thin photoanode of InSe/graphene heterostructure, *Nat. Commun.*, 2021, **12**, 91.

16 A. Ali, F. A. Mangrio, X. Chen, Y. Dai, K. Chen, X. Xu, R. Xia and L. Zhu, Ultrathin MoS_2 nanosheets for high-performance photoelectrochemical applications via plasmonic coupling with Au nanocrystals, *Nanoscale*, 2019, **11**, 7813–7824.

17 M. Yu, S. Zhao, H. Feng, L. Hu, X. Zhang, Y. Zeng, Y. Tong and X. Lu, Engineering Thin MoS_2 Nanosheets on TiN Nanorods: Advanced Electrochemical Capacitor Electrode

and Hydrogen Evolution Electrocatalyst, *ACS Energy Lett.*, 2017, **2**, 1862–1868.

18 L. Han, J. Luo, R. Zhang, W. Gong, L. Chen, F. Liu, Y. Ling, Y. Dong, Z. Yong, Y. Zhang, L. Wei, X. Zhang, Q. Zhang and Q. Li, Arrayed Heterostructures of MoS_2 Nanosheets Anchored TiN Nanowires as Efficient Pseudocapacitive Anodes for Fiber-Shaped Ammonium-Ion Asymmetric Supercapacitors, *ACS Nano*, 2022, **16**, 14951–14962.

19 Y. Wang, K. Liu, K. Huang, W. Wei, Y. Huang and H. Dai, Photothermal antibacterial MoS_2 composited chitosan hydrogel for infectious wound healing, *Biomater. Adv.*, 2024, **156**, 213701.

20 Y. Yang, Q. Fang, J. Wang, M. Li, Z. Li, H. Xu, S. Huang, J. Chen and B. Guo, Glucose–Activated Programmed Hydrogel with Self–Switchable Enzyme–Like Activity for Infected Diabetic Wound Self–Adaptive Treatment, *Adv. Mater.*, 2025, **37**, 2419158.

21 X. Zhang, C. Zhang, Y. Yang, H. Zhang, X. Huang, R. Hang and X. Yao, Light-assisted rapid sterilization by a hydrogel incorporated with Ag_3PO_4/MoS_2 composites for efficient wound disinfection, *Chem. Eng. J.*, 2019, **374**, 596–604.

22 B.-A. Chen, S. Ptasinska and P. V. Kamat, Metal Cocatalyst Dictates Electron Transfer in Ag-Decorated MoS_2 Nanosheets, *J. Phys. Chem. C*, 2022, **126**, 11907–11914.

23 Q. Hao, J. Liu, G. Wang, J. Chen, H. Gan, J. Zhu, Y. Ke, Y. Chai, J. Lin and W. Zhang, Surface-Modified Ultrathin InSe Nanosheets with Enhanced Stability and Photoluminescence for High-Performance Optoelectronics, *ACS Nano*, 2020, **14**, 11373–11382.

24 S. Wang, Y. Zhang, Y. Li, K. Chen, Y. Dai, D. Zhou, A. Ali, S. Yang, X. Xu, T. Jiang and L. Zhu, Au nanostars@PDA@Fe_3O_4-based multifunctional nanoprobe for integrated tumor diagnosis and photothermal therapy, *Mater. Des.*, 2021, **205**, 109707.

25 X. Xu, Q. Xu, W. Li, F. Xiao and H. Xu, From engineered photoactive materials to detection signal amplification strategies in photoelectrochemical biosensing of pathogens: New horizons and perspectives, *Chem. Eng. J.*, 2024, **480**, 147941.

26 L. Zou, L. Yang, Y. Zhan, D. Huang and B. Ye, Photoelectrochemical aptasensor for thrombin based on Au-rGO-CuS as signal amplification elements, *Microchim. Acta*, 2020, **187**, 433.

27 Y. Lei, K. Wang, S. Y. Wu, D. D. Huang, M. Dai, Y. J. Zheng, Z. L. Sun, Y. Z. Chen, X. H. Lin and A. L. Liu, 2′-Fluoro ribonucleic acid modified DNA dual-probe sensing strategy for enzyme-amplified electrochemical detection of double-strand DNA of PML/RARα related fusion gene, *Biosens. Bioelectron.*, 2018, **112**, 170–176.

28 Z.-Y. Zhang, L.-X. Huang, Z.-W. Xu, P. Wang, Y. Lei and A.-L. Liu, Efficient Determination of PML/RARα Fusion Gene by the Electrochemical DNA Biosensor Based on Carbon Dots/Graphene Oxide Nanocomposites, *Int. J. Nanomed.*, 2021, **16**, 3497–3508.

29 W. Zhang, X. Zheng and K. Jiao, Label-free and enhanced DNA sensing platform for PML/RARA fusion gene detection based on nano-ZnO functionalized carbon ionic liquid electrode, *Sens. Actuators, B*, 2012, **162**, 396–399.

30 N. Wei, J. Chen, J. Zhang, K. Wang, X. Xu, J. Lin, G. Li, X. Lin and Y. Chen, An electrochemical biosensor for detection of PML/RARA fusion gene using capture probe covalently immobilized onto poly-calcon carboxylic acid modified glassy carbon electrode, *Talanta*, 2009, **78**, 1227–1234.

31 J. Xie, J. Zhang, S. Li, F. Grote, X. Zhang, H. Zhang, R. Wang, Y. Lei, B. Pan and Y. Xie, Controllable Disorder Engineering in Oxygen-Incorporated MoS_2 Ultrathin Nanosheets for Efficient Hydrogen Evolution, *J. Am. Chem. Soc.*, 2013, **135**, 17881–17888.

32 N. K. Reddy, S. Winkler, N. Koch and N. Pinna, Electrochemical water oxidation of ultrathin cobalt oxide-based catalyst supported onto aligned ZnO nanorods, *ACS Appl. Mater. Interfaces*, 2016, **8**, 3226–3232.

33 X. Gao, X. Liu, Z. Zhu, Y. Gao, Q. Wang, F. Zhu and Z. Xie, Enhanced visible light photocatalytic performance of CdS sensitized TiO_2 nanorod arrays decorated with Au nanoparticles as electron sinks, *Sci. Rep.*, 2017, **7**, 973.

34 A. Ali, F. A. Mangrio, X. Chen, Y. Dai, K. Chen, X. Xu, R. Xia and L. Zhu, Ultrathin MoS_2 nanosheets for high-performance photoelectrochemical applications via plasmonic coupling with Au nanocrystals, *Nanoscale*, 2019, **11**, 7813–7824.

35 D. A. Reddy, J. Choi, S. Lee, Y. Kim, S. Hong, D. P. Kumar and T. K. Kim, Hierarchical dandelion-flower-like cobalt-phosphide modified CdS/reduced graphene oxide-MoS_2 nanocomposites as a noble-metal-free catalyst for efficient hydrogen evolution from water, *Catal. Sci. Technol.*, 2016, **6**, 6197–6206.

36 P. Y. Kuang, Y. Z. Su, K. Xiao, Z. Q. Liu, N. Li, H. J. Wang and J. Zhang, Double-Shelled CdS- and CdSe-Cosensitized ZnO Porous Nanotube Arrays for Superior Photoelectrocatalytic Applications, *ACS Appl. Mater. Interfaces*, 2015, **7**, 16387–16394.

37 J. M. Ball and W. Li, Using high-resolution microscopy data to generate realistic structures for electromagnetic FDTD simulations from complex biological models, *Nat. Protoc.*, 2024, **19**, 1348–1380.